

Nano-Scale Characterization of Particulate Iron Pyrite Morphology in Shale

Vasileios Angelidakis, Sadegh Nadimi,* Mohamed Garum, and Ali Hassanpour

This study analyzes the morphology of iron pyrite particles within a shale sample captured using nano-computed tomography (Nano-CT). The complex, framboidal morphology of the iron pyrite particles is characterized using various metrics, and comparisons are drawn on their effectiveness to quantify their observed morphological characteristics. Then, simplified representations of selected iron pyrite particles are generated to facilitate a sensitivity analysis of the effect of imaging resolution on morphological parameters of particle form. A discussion is developed on the required number of pixels per particle diameter for particle shape characterization. It is shown that shape indices that rely on the simplified main particle dimensions can be accurately calculated even for low fidelity levels of 10 pixels per particle diameter. More complex shape indices that use vertices, volume, and surface area, are more sensitive to image resolution, even for 40 pixels per particle diameter.

1. Introduction

Particulate materials appear across the scales (nano to macro) and in many industrial applications, our daily life, as well as in nature. They come with different physical attributes (size, shape, and surface properties) among which morphology, while very challenging to characterize, presents very special importance in numerous applications.^[1] In particular, the morphology of nano-particles is known to significantly influence their mechanical, chemical, rheological, and hydrologic behavior.^[2–7] For example, in nano biomaterials–cell interaction, particle shape affects the cellular functions in which effective morphology characterization would be central.^[8] In sedimentology, the chemical and morphological properties of nano-particles, e.g., pyrite, could be an indicator of historic environmental conditions that led to the formation of sedimentary basins.^[9] Notably, the morphology of pyrite influences the growth mecha-

nism of the structure of minerals within marine sediments.^[10] It has been shown that pyrite size distribution influences the redox condition in modern sediments.^[9] Furthermore, pyrite morphology and size have been used as an indicator of paleoredox conditions and shale gas content.^[11] Most recently, Khan et al.^[12] have used field emission electron scanning microscopy (FE-SEM) to characterize the size and morphology of iron pyrite within lacustrine shale to understand the mechanism of sediment formation (Figure 1). However, their study was limited to 2D characterization, which has been demonstrated to underrepresent the shape indices of irregular particles, as a single image of a particle is dependent on the current,


random particle orientation, and thus provides limited morphological information of the real, 3D morphology.

3D nano-scale shape characterization is challenging because of the limitation in measurement techniques and until recently the lack of openly available processing algorithms for the characterization of three-dimensional particles. Holzer et al.^[13] employed focused ion beam (FIB) nanotomography for morphology analysis and interface topology of ceramics, while Neubauer et al.^[14] analyzed the evolution of tricalcium silicate particle size during hydration using X-ray nano-tomography. However, these studies did not analyze 3D particle morphology characteristics rigorously.

To the best of the authors' knowledge, there is no previously reported 3D nano-computed tomography analysis of pyrite particles. In this work, we present for the first time a comprehensive analysis of morphology and size characterization of pyrite particles based on 3D X-ray Nano-computed Tomography of shale samples. Furthermore, the effect of image resolution in nano-scale morphology characterization is reported. This study can be extended to the characterization of nanomaterials that exhibit discrete granular structures in different applications, where limitations of measurement techniques, as opposed to the microscale, need to be taken into account when shape characteristics are analyzed and defined.

V. Angelidakis, S. Nadimi
School of Engineering
Newcastle University
Newcastle upon Tyne NE1 7RU, UK
E-mail: sadegh.nadimi-shahraki@ncl.ac.uk

M. Garum, A. Hassanpour
School of Chemical and Process Engineering
University of Leeds
Leeds LS2 9JT, UK

 The ORCID identification number(s) for the author(s) of this article can be found under <https://doi.org/10.1002/ppsc.202200120>.

© 2022 The Authors. Particle & Particle Systems Characterization published by Wiley-VCH GmbH. This is an open access article under the terms of the Creative Commons Attribution-NonCommercial License, which permits use, distribution and reproduction in any medium, provided the original work is properly cited and is not used for commercial purposes.

DOI: 10.1002/ppsc.202200120

2. Experimental Section

A small cubic core sample (25 μm side length) was prepared from reservoir rocks using a FIB milling technique.^[15] The sample preparation steps are shown in Figure 2. The sample was then characterized using ultra-high-resolution imaging by non-destructive X-ray nano-computed tomography (Nano-CT),

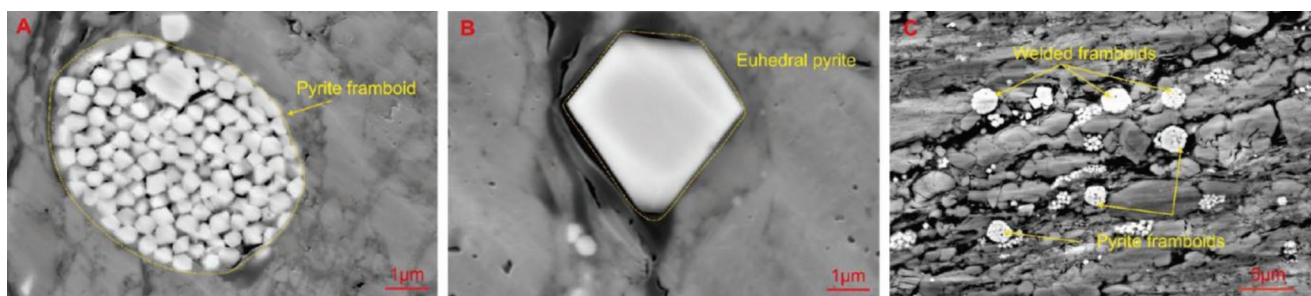


Figure 1. FE-SEM images representing the different types of pyrites employed to characterize the size and morphology of iron pyrite. Reproduced under terms of the CC-BY license.^[12] Copyright 2022, The Authors, published by American Chemical Society.

which resulted in a pixel size of 64 nm. The image size was $980 \times 1024 \times 1013$ with 16-bit depth. The scan was conducted at the National X-ray Computed Tomography (NXCT) research facility, University of Manchester.

The image post-processing steps are shown in Figure 3, including image binarization, filtering, and labeling. The contrast of the images is enhanced using the histogram stretching algorithm with 0.3% saturated pixel value in FIJI.^[16] Binarization is performed manually, based on the histogram of the full three-dimensional image, and not from individual image

slices. This course of action was employed to identify a single threshold intensity level for the whole sample.

The validity of particle shape characterization results became ambiguous for particles of low fidelity, as the extents of each particle become difficult to determine with certainty and neighboring particles can be misidentified as single particles, putting in danger the validity of the particle shape characterization at a bulk level. To avoid this and recognizing this limitation of the image-based particle characterization, a “characterization filter” was introduced to remove small particles from the shape

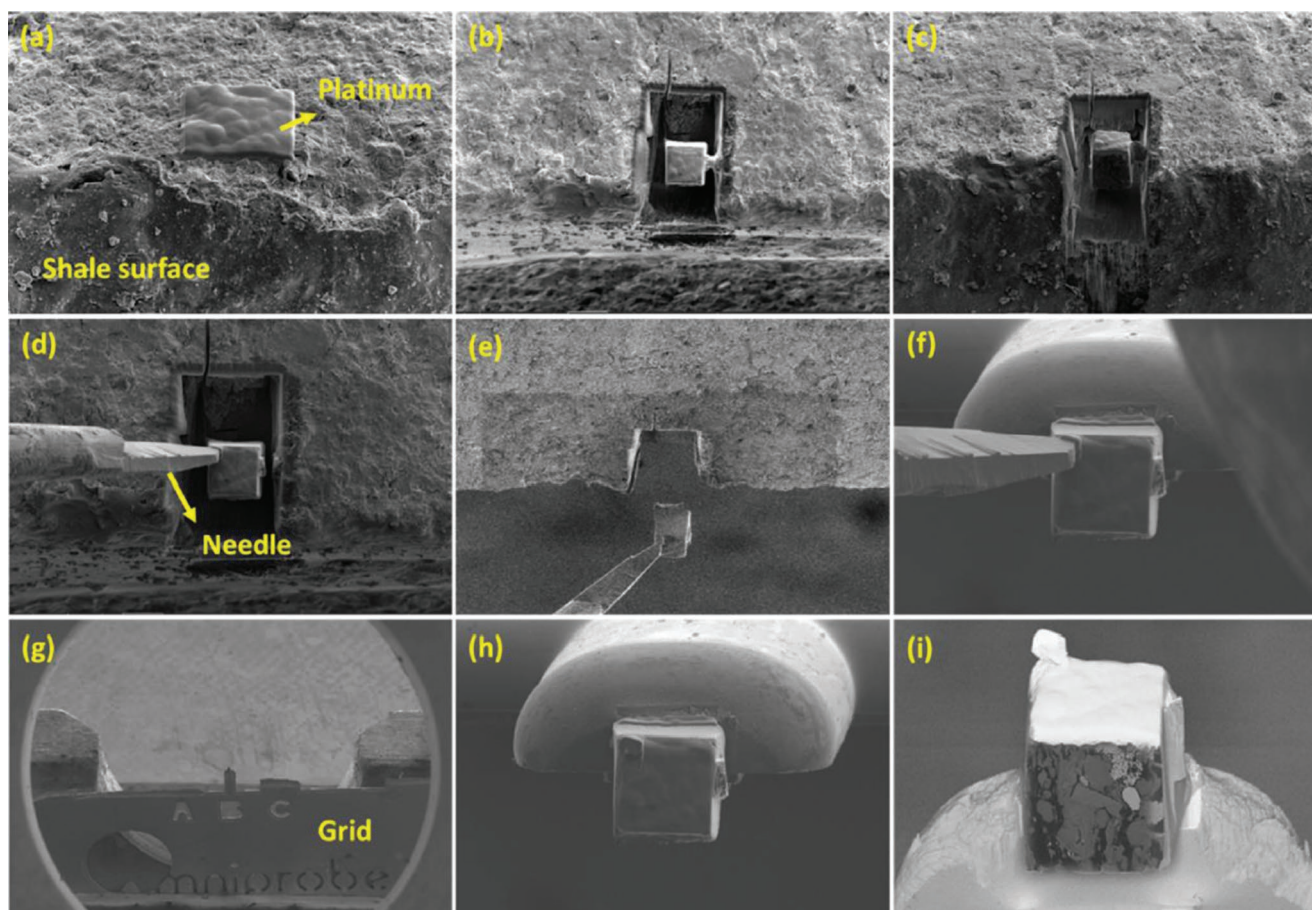


Figure 2. Shale rock sample prefor Nano-CT imaging, where the light gray, often small clusters, are iron pyrites: a) the surface of shale rock on which the region of interest is shown coated with Pt, b,c) mill out the area around the sample, d) attach the sample to the tip of a micromanipulator, e) cut the cube free from the bulk rock, and f–h) weld the bottom of the cylinder to the tip of a grid (here the samples are the small dark points on grid position B). i) Final sample (region of interest) is $\approx 25 \times 25 \mu\text{m}^2$. (Garum et al.^[15] with permission from ACS Publications).

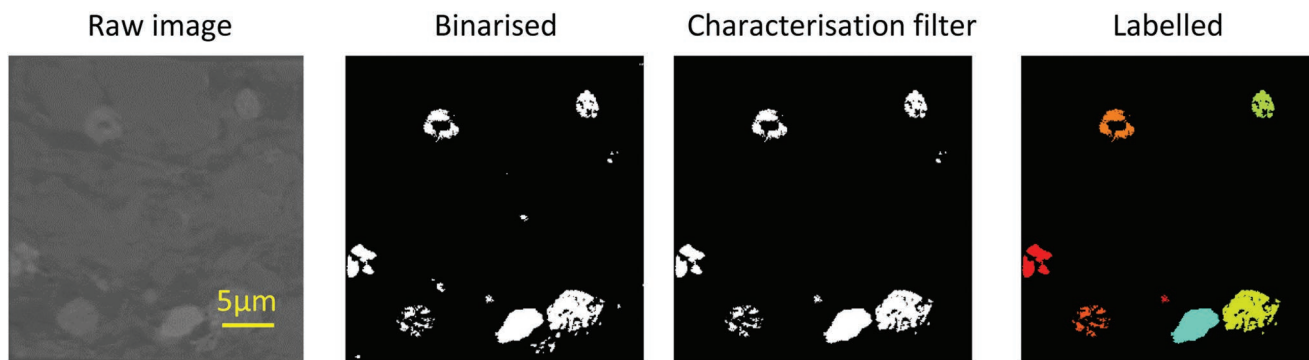


Figure 3. Image processing of shale Nano-CT images to isolate iron-pyrite granules.

characterization analysis, in relation to the pixel size used in this study. This was carried out aiming to characterize only particles the morphology of which was adequately captured by Nano-CT. Figure 4 shows the 3D rendering of the analyzed iron pyrites.

To this end, the volume of each particle was calculated, along with an equivalent sphere of equal volume and it was decided to remove particles corresponding to spheres with less than 15 pixels per diameter. This threshold was decided via visual inspections of the removed particles, which indeed seem of low quality and were prone to be affected by numerical noise introduced during binarization. This approach had an extra advantage, as it also removed numerical noise, leaving only the real iron pyrite particles to be characterized. A universal threshold value does not exist as different materials exhibit different degrees of morphological complexity.

The labeled image of the iron pyrite particles was imported in the open-source software *SHAPE: Shape Analyzer for Particle Engineering*,^[1] where they were processed in an automated manner. Each labeled voxelated image was imported in SHAPE, where it was transformed into a surface mesh, i.e., a triangulated tessellation of the particle surface, using a refined Delaunay triangulation algorithm.

The shape parameters analyzed in this study using SHAPE corresponded to larger morphological features, associated with particle form, since the image resolution did not allow for a characterization of finer features associated with roundness and angularity, for these particle sizes. Convexity was calculated as the ratio of the particle volume over the volume of its convex hull. The degree of true sphericity was calculated as in Wadell,^[17] as the ratio of the surface area of a sphere with equal volume as the particle to the actual surface area of the particle. Intercept sphericity

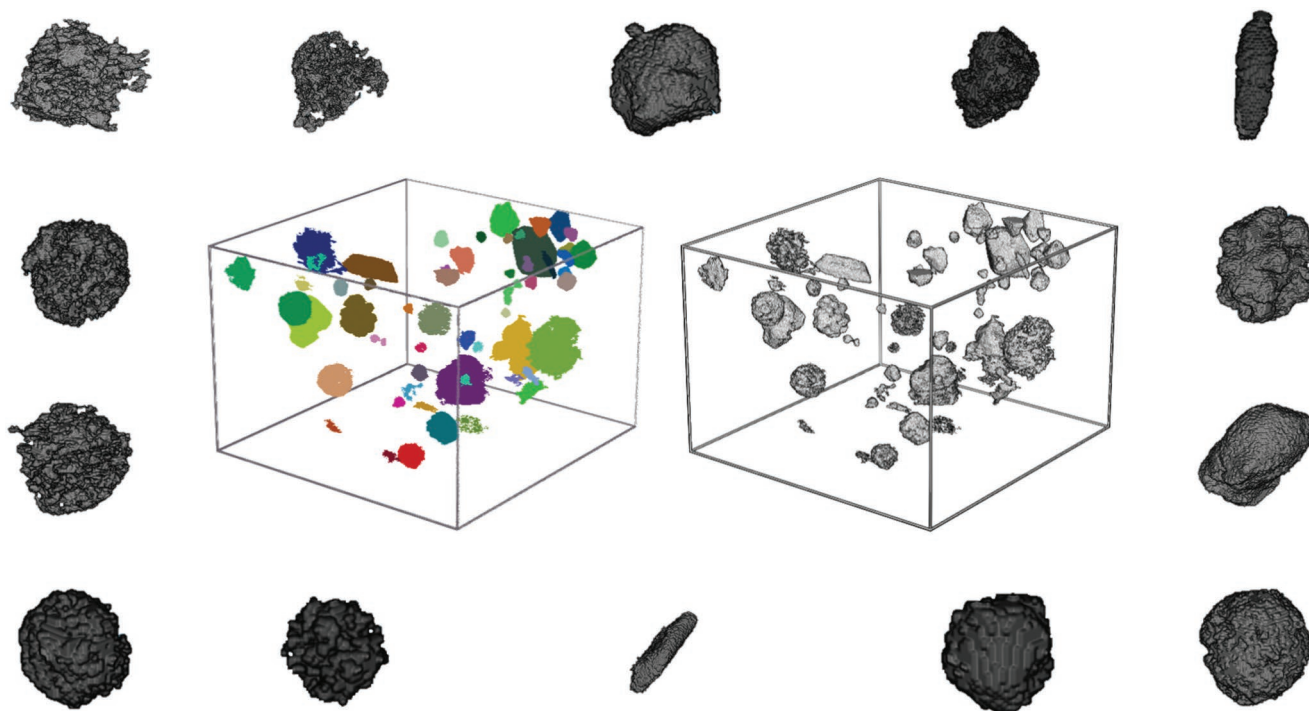


Figure 4. 3D reconstructed Nano-CT images. The labeled and grayscale images of the full sample are shown in the center, surrounded by selected magnified iron pyrite particles.

was calculated as in Krumbein,^[18] involving the three main particle dimensions. The main particle dimensions, also known as the *Feret* dimensions, were calculated using two methods, as the axes of an ellipsoid fitted to the particle vertices using non-linear least squares and using the minimal volume-oriented bounding box of the particle vertices. Flatness and elongation were calculated using the formulation of Angelidakis et al.,^[19] which make use of the main particle dimensions as well. The formulae used to calculate each shape parameter can be found in the Appendix. These indices took values within the range (0,1], demonstrating percentile values of each analyzed morphological feature.

3. Results and Discussion

3.1. Shape Characteristics of Iron Pyrite

For a given volume, a sphere is the geometrical shape with the smallest possible surface area. The more complex the particle surface, i.e., the more it deviates from a sphere, the larger the surface area and the smaller the degree of true sphericity. A particle can deviate from a sphere either in terms of form, e.g., by being flat, elongated or bladed (both flat and elongated) or by the complexity of its surface topography, i.e., the existence of local asperities or concavities, which also increase the surface area.

The analyzed iron-pyrite particles demonstrate a wide range for all employed shape parameters, because of their complex morphology. As shown in Table 1, the convexity index demonstrates a full range of results, from very concave to very convex particles.

To monitor particle sphericity and flatness and elongation for the iron pyrites, the values of each parameter are plotted on top of a *Zingg plot*. Zingg^[20] proposed an intuitive visualization of particle form, plotting two aspect ratios c/b against b/a , in what is widely referred to as a *Zingg plot*, where $a > b > c$ the

Table 1. Shape parameters of iron-pyrite particles.

Parameter	Minimum	Maximum	Mean	Median
Convexity	0.046	0.895	0.596	0.693
Degree of true sphericity	0.079	0.437	0.297	0.308
Intercept sphericity (OBB)	0.439	0.989	0.783	0.791
Intercept sphericity (ELL)	0.095	0.924	0.611	0.651
Flatness (OBB)	0.004	0.504	0.129	0.095
Elongation (OBB)	0.005	0.407	0.122	0.074
Flatness (ELL)	0.01	0.742	0.234	0.187
Elongation (ELL)	0.031	0.670	0.207	0.140

main particle dimensions. Angelidakis et al.^[19] recently proposed a new classification system for particle form, which they plotted on top of a Zingg plot.

The degree of true sphericity shows relatively low values, because of the framboidal nature of the majority of particles. On the other hand, intercept sphericity shows higher values, as it relies on the main particle dimensions and is not affected by the surface area. As a result, it can be argued that intercept sphericity does not actually show sphericity, i.e., the degree of resemblance to a sphere, but instead shows compactness, as compact framboidal particles will have a low degree of true sphericity and high intercept sphericity values (see Figure 5). The flatness (*fl*) and elongation (*e*) indices demonstrate a narrow range of results, with both their average and median results below the value of 0.2 (i.e., $fl < 0.2$ and $el < 0.2$), indicating that most particles are compact (Figure 6). This is in agreement with the high values of intercept sphericity. Non-compact particles can be either flat, elongated or bladed and several classification systems of particle form have been proposed in the literature. Figure 6c shows a classification of these particles using the recently proposed

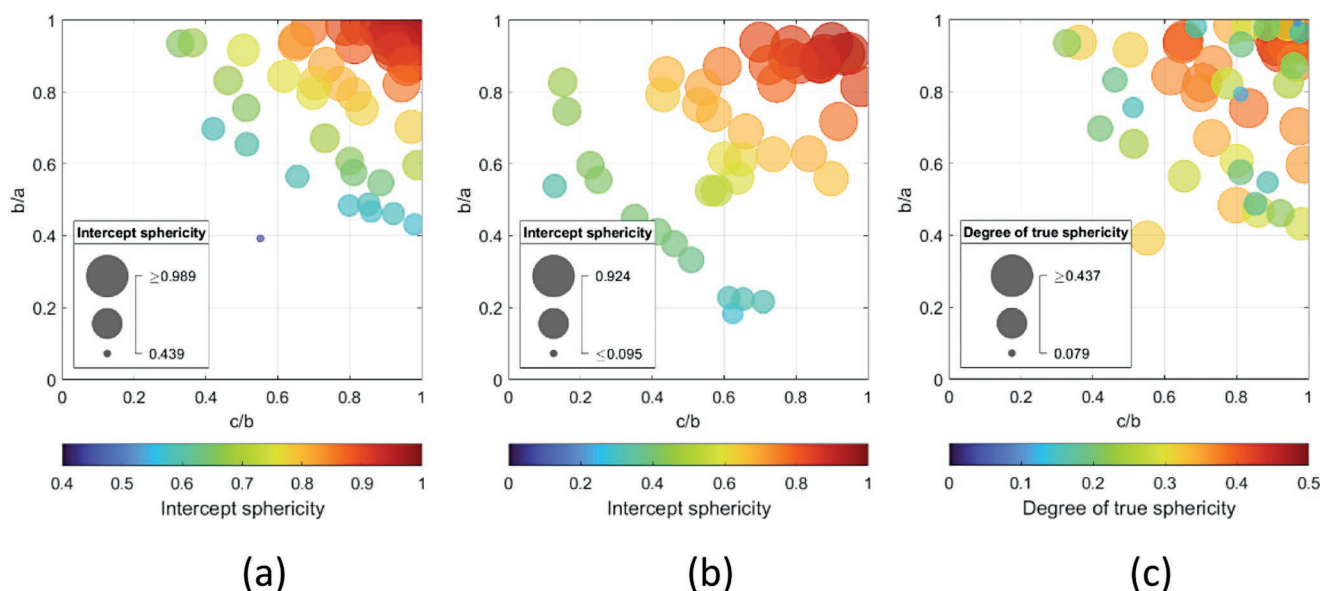


Figure 5. Various measures of sphericity. a) Intercept sphericity using the main particle dimensions of the oriented bounding box, b) Intercept sphericity using the dimensions of the fitted ellipsoid, c) Degree of true sphericity. The main particle dimensions in (a,c) are calculated based on the oriented bounding box, while in (b) based on a fitted ellipsoid.

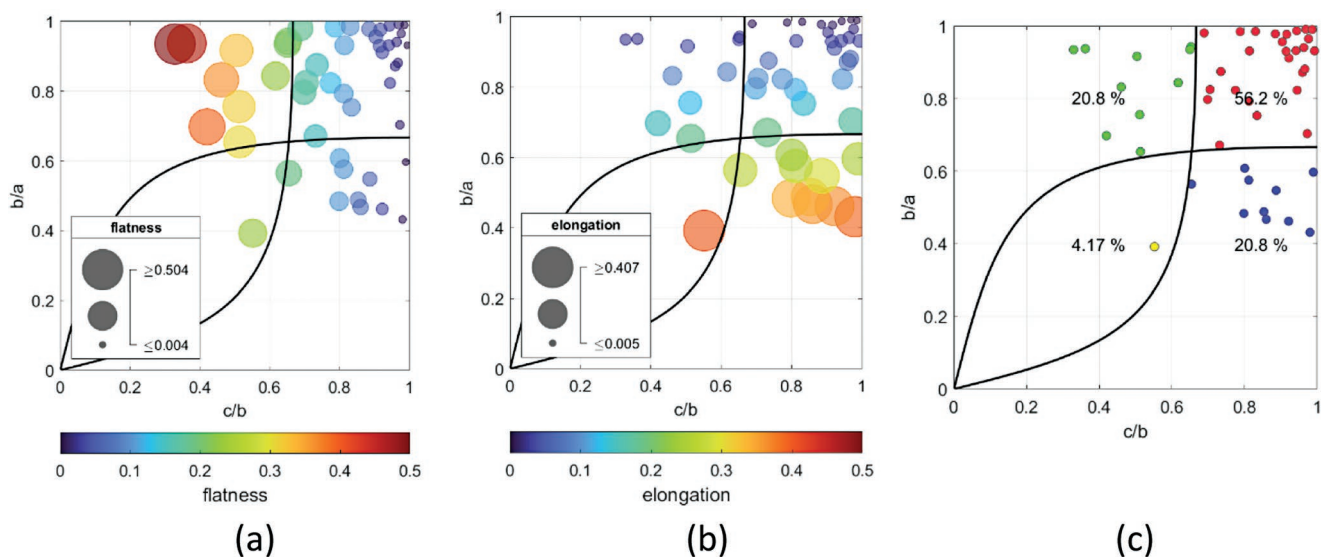


Figure 6. Characterization and classification of iron pyrite particles using the dimensions of a minimal bounding box (OBB): a) flatness; b) elongation; c) classification into flat (green), compact (red), bladed (yellow), and elongated (blue) particles with corresponding percentages 20.8%, 56.2%, 4.17%, and 20.8%. The bold lines correspond to the boundaries among classes, according to the classification system of Angelidakis et al.^[9]

system of Angelidakis et al.,^[9] and the main particle dimensions according to the oriented bounding box, into flat (20.8%), compact (56.2%), bladed (4.17%), and elongated (20.8%).

For most indices, the results from using the oriented bounding box present similar values to the ones from using the fitted ellipsoid. Only intercept sphericity shows a very low value for the fitted ellipsoid case. It is reminded that although the minimal oriented bounding box is not affected by the internal structure of the particle, only by its outer extents, the fitted ellipsoid is calculated using all particle vertices. In SHAPE, different vertices can be used for this fitting, e.g., using the vertices only at the surface of the particle, of a tetrahedral mesh of the particle or else the points corresponding to all the voxels making the particle. Here, the points corresponding to the voxels making the particle are considered to calculate the ellipsoid, aiming to get more information on the form of these complex particles.

The main particle dimensions demonstrate small values, in the threshold of the nano and micron scale. The smallest particle dimension is about a fourth of a micron and the large one is less than 9 μm . In more detail, the particle dimensions vary from 0.387 to 6.482 μm according to the minimal oriented bounding box and from 0.276 to 8.445 μm according to a fitted ellipsoid. The full set of shape parameters is presented in Table 1 using both the oriented bounding box and fitted ellipsoid to facilitate comparisons. **Figure 7** shows the range of main particle dimensions, estimated as the dimensions of an oriented bounding box (OBB) and a fitted ellipsoid (ELL).

3.2. Effect of Image Resolution on Shape Parameters

The accuracy of particle size and shape characterization is directly affected by the resolution of the images capturing the shape of each particle. Five iron-pyrites are simplified to decreasing fidelity levels, where fidelity is quantified using the “pixel per diameter (ppd)” index.

To generate simplified versions of the particles corresponding to each fidelity level, image resampling is carried out in Matlab, where the size of each image is reduced by a scale factor. To create comparable results, all five particles are brought to the same initial fidelity level (40 pixels per particle diameter). For a given particle, the sphere of equal volume is calculated and its radius is recorded. Then, a sphere is calculated for each fidelity level, considering 40, 25, 15, and 10 pixels per diameter. The scale factor (SF) is calculated as the ratio of the sphere radius for each simplified level over the radius of equivalent sphere at the original fidelity level:

$$SF = \frac{r_{\text{target}}}{r_{\text{original}}} = \sqrt[3]{\frac{V_{\text{target}}}{V_{\text{original}}}} \quad (1)$$

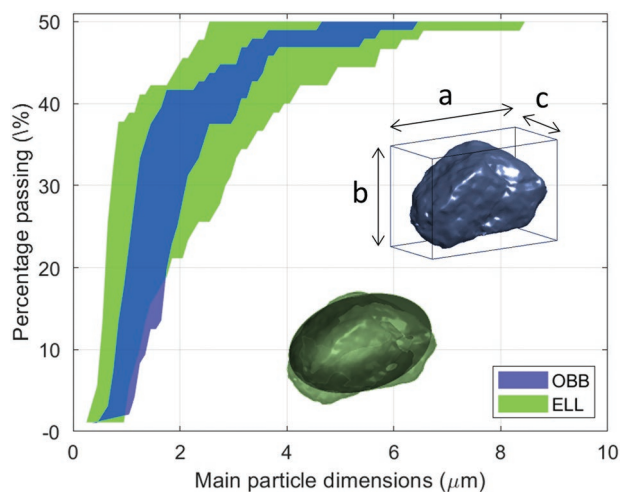
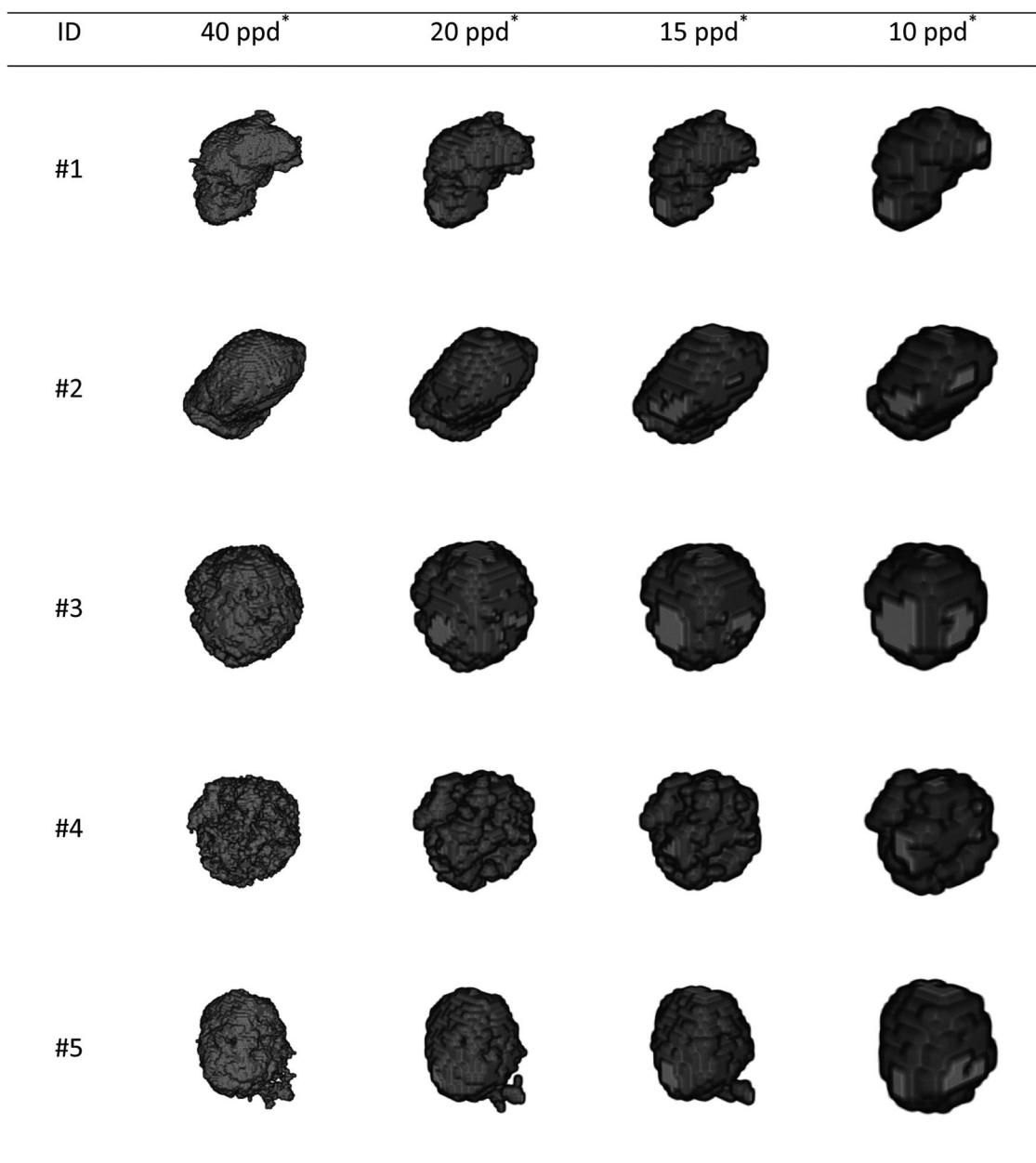


Figure 7. Range of main particle dimensions, estimated as the dimensions of an oriented bounding box (OBB) and a fitted ellipsoid (ELL). Inset: Main particle dimensions ($a > b > c$) using a minimal bounding box (blue) and a fitted ellipsoid (green).



* ppd: pixels per diameter.

Figure 8. Iron-pyrite particles for decreasing fidelity levels.

where r_{target} , r_{original} , V_{target} , V_{original} , the radius and volume of each target (simplified) and the original fidelity level.

Having established a technique to calculate the scale factor, image resampling is implemented using a nearest-neighbor interpolation technique to calculate the intensity of each voxel in each simplified fidelity level. The resampled grayscale image is then binarized using the thresholding method of Otsu.^[21] **Figure 8** shows the morphology of the five simplified particles for the four fidelity levels. It can be observed that as particle morphology is simplified, finer characteristics of the particle surface topography get eliminated, as expected.

Figure 9 presents a quantitative analysis of particle shape for all the analyzed fidelity levels. It becomes evident that convexity is sensitive to the simplification of fidelity for the particles that are initially concave, as the simplified particles tend to become more convex. The flatness, elongation, compactness and intercept sphericity values are only presenting minimal variations, and their values are preserved even for 10 pixels per diameter. The same cannot be said for the degree of true sphericity, which presents a steep increase for particles with small initial values, and a milder increase for particles with high initial values, for decreasing fidelity. Conceptually, higher fidelity can capture the framboidal, highly fractal topography of the iron pyrite parti-

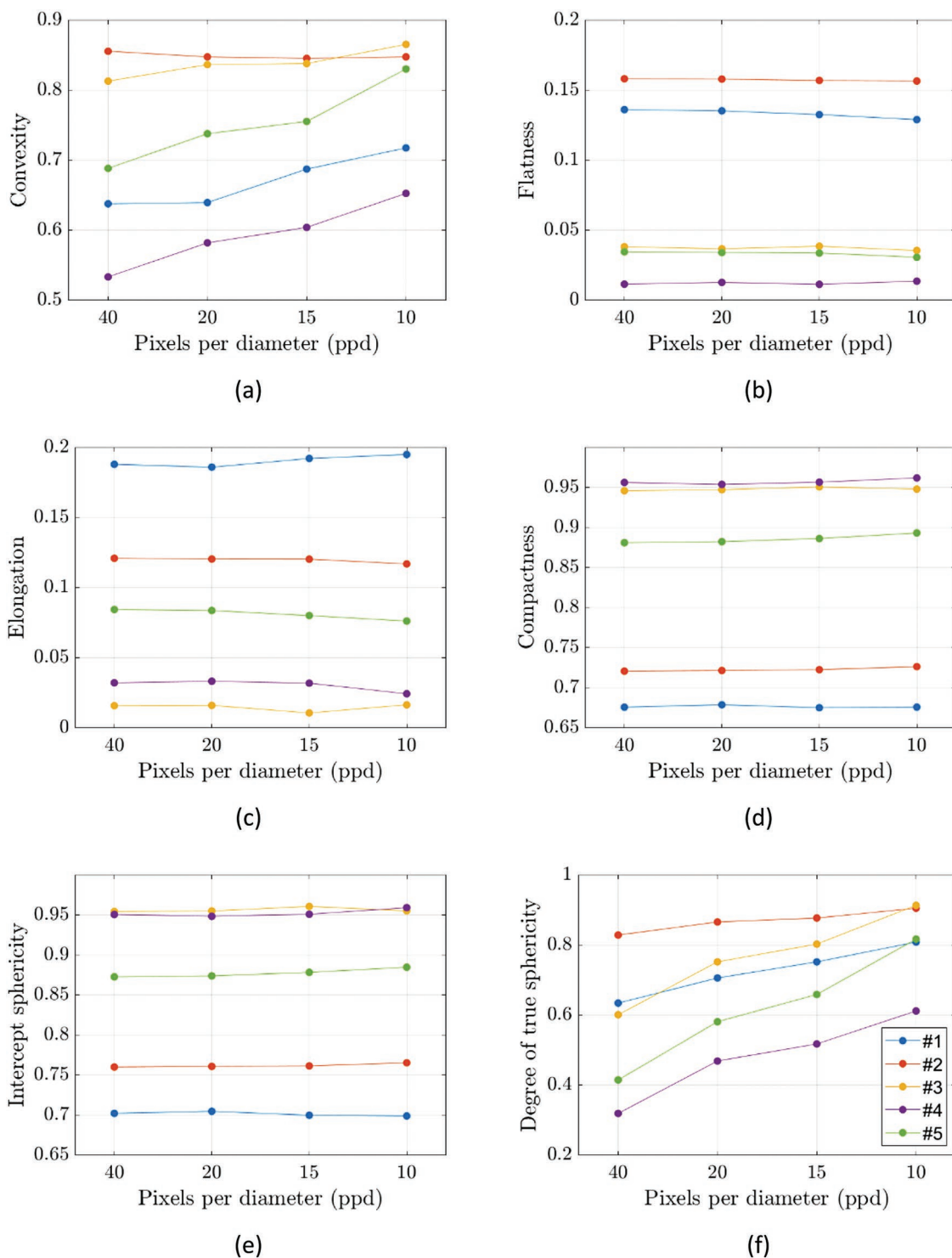


Figure 9. Shape characterization of the particles in Figure 8 for various fidelity levels a) convexity, b) flatness, c) elongation, d) compactness, e) intercept sphericity, f) degree of true sphericity.

cles, which have increased surface area, while for decreasing fidelity these features get less represented, a decreased surface area is recorded for small volume changes and thus the degree of true sphericity increases. This becomes evident if we compare particles #1 and #4 in Figure 8; particle #4 seems more

equant, but highly framboidal at the 40 ppd fidelity level, and its degree of true sphericity is lower than particle #1, as seen in Figure 9, even though particle #1 is much less equant. This reveals a limitation of the degree of true sphericity to capture the overall resemblance of a particle to a sphere, as it is affected

both by particle form and roundness,^[22] where “form” refers to a first degree approximation of particle morphology, regarding the overall shape of the particle, while “roundness” refers to a second degree approximation of particle morphology, pertaining to smaller features on the particle surface.

It can be asserted that the shape indices that rely on the actual particle morphology, like convexity and degree of true sphericity, which rely on the particle vertices, volume, and surface area respectively, are more sensitive to the simplification of fidelity. On the other hand, the indices calculated using the main particle dimensions, in this example calculated as the axes of a fitted ellipsoid, are not sensitive to the simplification of fidelity and can thus lead to adequate shape characterization even for low-quality images, as long as the actual extents of the particle are identified, i.e., as long as the particle is not considered to be agglomerated to its neighboring particles during image segmentation.

Interesting to note that the values of intercept sphericity for these five particles shows close similarity to their values of compactness across fidelity levels. This similarity was also identified in the previous section at the scale of the full sample.

Additional to image resolution in terms of pixels per diameter, there are other sources of deficiency to characterize particles fr. Shape characterization of 3D images of an ellipsoid with various levels of noise and blur, varied in a parametric manner, showed that image quality affected the obtained morphological results by as much as 25%, for the analyzed range of parameters.^[1]

4. Concluding Remarks

This study aimed to provide insights into the complex morphology of iron pyrites at the nano-scale by means of quantitative particle shape characterization. The size and main particle dimensions were calculated using both the minimal oriented bounding boxes and fitted ellipsoids of the particles, to facilitate comparisons, with the dimensions of the fitted ellipsoid leading to a wider range of results. The complex, framboidal structure of some particles resulted in increased surface area in regards to their volume and in turn led to decreased values of true sphericity, which is calculated based on the particle volume and surface area. On the other hand, the intercept sphericity is calculated based on the three main particle dimensions and is not affected directly from the complex particle surface topography. Though, intercept sphericity does not distinguish between ellipsoids and cuboids, and is thus reflecting a metric of particle compactness, rather than particle sphericity. A parametric study was conducted, characterizing the shape of five iron pyrite particles for decreasing fidelity levels. It was found that shape indices relying on the simplified main particle dimensions are less sensitive to simplification, and can be calculated robustly even for 10 pixels per particle diameter. On the other hand, indices relying on the particle vertices, volume and surface area were more sensitive to shape simplification, even for 40 pixels per particle diameter. Extension of this work to other applications would be useful in 3D characterization of nano material morphology, where the resolution of the measurement techniques could limit data acquisition and analysis.

Table 2. Formulae of shape parameters.

Shape parameter	Formula	Comments
Convexity	$V = \frac{V}{V_{CH}}$	V: Particle volume V _{CH} : Volume of convex hull
Degree of true sphericity ^[17]	$\Psi = \frac{\sqrt[3]{36\pi V^2}}{A}$	A: Particle surface area
Intercept sphericity ^[18]	$\Psi_{int} = \sqrt[3]{\frac{b \cdot c}{a^2}}$	a, b, c: Main particle dimensions (long, intermediate, short)
Flatness ^[19]	$fl = \frac{b^2}{a \cdot c + b^2} - \frac{c}{a + c}$	
Elongation ^[19]	$el = \frac{a \cdot c}{a \cdot c + b^2} - \frac{c}{a + c}$	
Compactness ^[19]	$co = \frac{2 \cdot c}{a + c}$	

5. Appendix: Formulae Used for Particle Shape Characterization

Particle shape characterization is a scientific field challenged by subjectivity and high user-dependency, as several different shape parameters have been proposed in the literature to quantify similar aspects of particle shape. **Table 2** details the formulations employed to calculate the shape parameters in this study.

Acknowledgements

This work was supported by the Engineering and Physical Sciences Research Council (Grant No. EP/R511584/1) entitled “OCULAR: automated acquisition and classification of particles.” The authors would like to thank the Leeds University Electron Microscopy and Spectroscopy Center (LEMAS) for technical support (Stuart Micklethwaite) and John Wynn Williams of Leeds University School of Earth and Environment for sample preparation. The authors would like to also acknowledge the support of the Henry Royce Institute through the Royce Ph.D. Equipment Access Scheme enabling access to facilities at Royce@Manchester; EPSRC Grant Number EP/19/0044.

Conflict of Interest

The authors declare no conflict of interest.

Data Availability Statement

The data that support the findings of this study are available from the corresponding author upon reasonable request.

Keywords

iron pyrite morphology, nano-computed tomography, particle shape characterization

Received: June 20, 2022
Revised: September 15, 2022
Published online: November 9, 2022

- [1] V. Angelidakis, S. Nadimi, S. Utili, *Comput. Phys. Commun.* **2021**, 265, 107983.
- [2] A. R. Tao, S. Habas, P. Yang, *Small* **2008**, 4, 310.
- [3] J. Ren, R. D. Tilley, *Small* **2007**, 3, 1508.
- [4] H. Canziani, S. Chiera, T. Schuffenhauer, S. P. Kopp, F. Metzger, A. Bück, M. Schmidt, N. Vogel, *Small* **2020**, 16, 2002076.
- [5] Y. Du, W. Weng, Z. Zhang, Y. He, J. Xu, J. Sun, J. Liao, J. Bao, X. Zhou, *ACS Mater. Lett.* **2021**, 3, 356.
- [6] A. Lüken, L. Stüwe, S. B. Rauer, J. Oelker, J. Linkhorst, M. Wessling, *Small* **2022**, 18, 2107508.
- [7] Y. Xu, J. Li, J. Sun, L. Duan, J. Xu, D. Sun, X. Zhou, *J. Colloid Interface Sci.* **2022**, 615, 840.
- [8] R. Augustine, A. Hasan, In *Handbook of Biomaterials Biocompatibility*, Woodhead Publishing, UK **2020**, pp. 473–504.
- [9] R. T. Wilkin, H. L. Barnes, S. L. Brantley, *Geochim. Cosmochim. Acta* **1996**, 60, 3897.
- [10] K. Liu, F. Huang, S. Gao, Z. Zhang, Y. Ren, B. An, *Ore Geol. Rev.* **2022**, 141, 104630.
- [11] Z. Liu, D. Chen, J. Zhang, X. Lü, Z. Wang, W. Liao, X. Shi, J. Tang, G. Xie, *Minerals* **2019**, 9, 428.
- [12] D. Khan, L. Qiu, C. Liang, K. Mirza, S. U. Rehman, Y. Han, A. Hannan, M. Kashif, K. L. Kra, *ACS Omega* **2022**, 7, 1244.
- [13] L. Holzer, B. Muench, M. Wegmann, P. Gasser, R. J. Flatt, *J. Am. Ceram. Soc.* **2006**, 89, 2577.
- [14] J. Neubauer, T. Sowoidnich, L. Valentini, C. Schulbert, C. Naber, C. Rößler, J. DaSilva, F. Bellmann, **2022**, *Cem. Concr. Res.* 156, 106769.
- [15] M. Garum, P. W. Glover, P. Lorinczi, G. Scott, A. Hassanpour, *Energy Fuels* **2020**, 35, 702.
- [16] J. Schindelin, I. Arganda-Carreras, E. Frise, V. Kaynig, M. Longair, T. Pietzsch, A. Cardona, *Nat. Methods* **2012**, 9, 676.
- [17] H. Wadell, *J. Geol.* **1932**, 40, 443.
- [18] W. C. Krumbain, *J. Sediment. Res.* **1941**, 11, 64.
- [19] V. Angelidakis, S. Nadimi, S. Utili, *Powder Technol.* **2022**, 396, 689.
- [20] T. Zingg, *Doctoral dissertation*, ETH Zurich, **1935**.
- [21] N. Otsu, *IEEE Trans. Syst. Man Cybern.* **1979**, 9, 62.
- [22] S. J. Blott, K. Pye, *Sedimentology* **2008**, 55, 31.